Journal of Catalysis 399 (2021) 67–74

Contents lists available at ScienceDirect

Journal of Catalysis

journal homepage: www.elsevier.com/locate/jcat

Electrochemical reduction of SnO_2 to Sn from the Bottom: In-Situ formation of SnO_2/Sn heterostructure for highly efficient electrochemical reduction of carbon dioxide to formate

Shunlian Ning [a], Jigang Wang [a], Dong Xiang [a], Shaobin Huang [a], Wei Chen [b], Shaowei Chen [c,1,*], Xiongwu Kang [a,1,*]

[a] School of Environment and Energy, South China University of Technology, Higher Education Mega Center, 382 East Waihuan Road, Guangzhou 510006, China
[b] State Key Laboratory of Electroanalytical Chemistry, Changchun Institute of Applied Chemistry, Chinese Academy of Sciences, Changchun, 130022, China
[c] University of California, Santa Cruz, 1156 High Street, CA, 95064 USA

ARTICLE INFO

Article history:
Received 8 January 2021
Revised 15 April 2021
Accepted 26 April 2021
Available online 7 May 2021

Keywords:
electrochemical CO_2 reduction
In-situ reconstruction
operando Raman spectroscopy
SnO_2/Sn heterostructures
Formate
DFT calculations

ABSTRACT

Design and engineering of low-cost, high-performance catalysts is a critical step in electrochemical CO_2 reduction (CO_2R) to value-added chemicals and fuels. Herein, SnO_2 nanoparticles were grown onto carbon cloth (SnO_2/CF) by a facile hydrothermal procedure and exhibited excellent electrocatalytic activity towards CO_2R due to reconstruction into SnO_2/Sn Mott-Schottky heterojunctions during CO_2R electrolysis, as manifested in X-ray diffraction, X-ray photoelectron spectroscopy, and operando Raman spectroscopy measurements. The heterostructured SnO_2/Sn electrode delivered a high faradaic efficiency of 93 ± 1% and a partial current density of 28.7 mA cm^{-2} for formate production at − 1.0 V vs. reversible hydrogen electrode in an H-type cell (which remained stable for 9 h), and 174.86 mA cm^{-2} at − 1.18 V on a gas-diffusion electrode in a flow cell. Density functional theory calculations show that the SnO_2/Sn heterostructures in situ formed under CO_2R conditions helped decrease the energy barrier to form formate as compared to pristine SnO_2 and Sn, and were responsible for the high activity and selectivity of formate production. Results from this study unravels the evolution dynamics of SnO_2 catalysts under CO_2R condition and provides a further understanding of the active component of SnO_2 catalyst in CO_2R.

1. Introduction

Electrochemical carbon dioxide (CO_2)reduction (CO_2R) to value-added industrial chemicals and liquid fuels is an effective strategy to alleviate the greenhouse issues and achieve the carbon neutral cycle.[1-3] Among the molecules produced from CO_2R, formate is considered as an important product, since it can be used as fuels for direct formic acid fuel cell.[4] Yet, as CO_2 is a chemically inert molecule, the conversion from CO_2 to formate typically entails a high energy barrier, and the reaction can be complicated by the competitive hydrogen evolution reaction (HER).[5,6] Within this context, it is critical to develop efficient catalysts for CO_2R that can lower the overpotential and improve the activity and selectivity towards formate.

SnO_2 is an n-type semiconductor, and has been widely recognized as an excellent electrocatalyst for CO_2R to formate, where the catalytic activity is strongly dependent on the electronic and geometric properties of the catalysts.[7-10] For example, Li et al. prepared self-assembled microporous SnO_2 nanosheets and observed a Faraday efficiency (FE) of 83% for formate production at a low overpotential of −710 mV. In another study, Spurgeon et al. synthesized porous SnO_2 nanowires with rich grain boundaries, which achieved an FE of 78% for formate production at –0.8 V vs RHE.

However, it has been noticed that SnO_2 cannot survive under the electrochemical condition of CO_2R. Kanan et al.[11] speculated that SnO_2 might be partially reduced to Sn and form a metal/semiconductor heterojunction during the CO_2R. The electronic interaction and charge transfer at the SnO_2/Sn interface, the so-called Mott–Schottky effect, is responsible for the high performance of CO_2R[12] In addition, since SnO_2 is prone to be reduced into Sn under the CO_2R condition, it has also been argued that either SnO_2 or Sn is the actual active component for CO_2R. Thus, to unravel the CO_2R mechanism on SnO_2, it is necessary to understand the structural dynamics of SnO_2 during the electrochemical operation.

Herein, SnO_2 nanoparticles were grown onto carbon cloth by a facile hydrothermal procedure. During CO_2R electrocatalysis,

* Corresponding authors.
E-mail addresses: shaowei@ucsc.edu (S. Chen), esxkang@scut.edu.cn (X. Kang).
[1] These authors contribute equally to the paper.

https://doi.org/10.1016/j.jcat.2021.04.028
0021-9517/

SnO_2 was partially reduced to Sn from the bottom of the resulting SnO_2/CF composite, forming SnO_2/Sn heterostructure, as evidenced in by X-ray diffraction (XRD), in situ Raman spectroscopy and X-ray photon electron spectroscopy (XPS) measurements. Density functional theory (DFT) calculations show that the SnO_2/Sn heterostructure enhanced the stability of the *HCOO intermediate, as compared to pure SnO_2 and Sn, and led to highly selective production of formate.

2. Experimental

2.1. Materials

Tin (II) chloride ($SnCl_2{\cdot}2H_2O$, 99% purity, Sinopharm Chemical Reagents Co., Ltd., China), urea (CH_4N_2O, 97%, Energy Chemicals), Nafion (0.5 wt%, Alfa Aesar). Ethanol (99%, Tianjin Damao Chemical Works)), acetic acid (99.5%, Tianjin Damao Chemical Works), formic acid (88%, Tianjin Damao Chemical Works), and carbon black (Vulcan XC-72, Cabot) were used as received without further treatment. Deionized water was obtained from a Barnstead Nanopure water system (18.2 MΩ•cm).

2.2. Preparation of SnO_2/CF and Sn/CF catalysts

A facile hydrothermal method was employed to synthesize SnO_2 on carbon cloth. In a typical experiment, an aqueous solution of $SnCl_2{\cdot}2H_2O$ (18.5 mmol L^{-1}) was added to an ethanol and water mixture (v:v = 1:1) to form a white turbid suspension, into which was then added 0.48 g of urea, leading to a change of the solution color from white to yellow. The solution was magnetically stirred for 10 min and transferred into a Teflon–lined autoclave hydrothermal reactor, which contained a piece of carbon cloth (3 cm × 3 cm), and heated at 120 °C for 10 h. After cooling to room temperature, the precipitate (SnO_2/CF) was collected by centrifugation, washed with deionized water several times, dried at 50 °C overnight, and directly used for electrochemical reduction of CO_2. As a control experiment, Sn/CF was prepared by calcining the obtained SnO_2/CF at 600 °C for 4 h under an Ar/H_2 (with 10% H_2) atmosphere.

2.3. Characterization

The morphology of the catalysts prepared above was characterized by using scanning electron microscopy (SEM, Hitachi S-4800) and high–resolution transmission electron microscopy (HRTEM, JEOL JEM 2100F) measurements. The crystalline structure and surface chemical compositions of the samples were analyzed by using X-ray diffraction (XRD, New D8 – Advance, BRUKER–AXS) at a scan rate of 5° min^{-1}, and X–ray photoelectron spectroscopy (XPS, Thermo Fisher Scientific, K – alpha +), respectively.

2.4. Electrochemistry

All electrochemical experiments were conducted with a CHI 660C electrochemical work-station in a three-electrode setup in an H-type cell, with the two compartments separated by a Nafion-117 membrane to prevent the re-oxidation of CO_2 reduction products. The SnO_2/CF prepared above was used as the working electrode, a Pt wire as the counter electrode, and a Ag/AgCl reference as the reference electrode. The reference electrode was calibrated against a reversible hydrogen electrode (RHE) and all potentials in the present study were referred to this RHE unless otherwise stated. A CO_2-saturated 0.5 M $KHCO_3$ solution (pH = 8.3) was used as the supporting electrolyte.

Prior to electrochemical measurements, the electrolyte in the cathodic compartment was saturated with CO_2 by bubbling CO_2 gas for at least 30 min. During the electrochemical reduction experiments, the CO_2 gas was delivered at an average rate of 25 mL min^{-1} (at ambient condition) and routed directly into the gas sampling loop of a gas chromatograph (GC 9560) for quantification of the gas products. The GC was installed with a thermal conductivity detector (TCD) to detect H_2 and flame ionization detector (FID) to detect hydrocarbons. A methanizer (Agilent) was equipped in front of the FID for CO detection. High-purity Ar was used as the carrier gas for all compartments of the GC. The liquid products of CO_2R were identified and quantified by nuclear magnetic resonance (NMR, 400 MHz, Bruker) measurements.

The Faradaic efficiency was calculated by employing the following equation:

$$FE = \frac{Q_i}{Q_{total}} = \frac{nN_iF}{Q_{total}}$$

where Q_{total} is the total charge passed, Q_i is the charge for a certain CO_2R product, N_i is the number of moles of a specific product (measured by NMR and GC), n is the number of electrons exchanged for product formation (n = 2 for CO, H_2 and formate), and F is the Faradaic constant (96485C mol^{-1}).

2.5. Computational studies

Plane-wave density functional theory (DFT) calculations were performed by using the CASTEP code of the Materials Studio package of Acclerys Inc[13]. The dispersion correction was considered through zero damping DFT-D3 method[14]. In all calculations, the spin polarized generalized gradient approximation (GGA) of the Perdew–Burke–Ernzerhof (PBE) functional[15] and ultrasoft pseudo-potentials were used for the core electrons. The calculations were conducted on SnO_2(1 1 0) or Sn (1 1 2) surface with four stoichiometric layers, respectively, by using a 3 × 2 periodic cells with an optimized vacuum space of 20 Å, where the atoms in the two bottom layers were fixed and those in the upper layers were allowed to fully relax in the calculations. The SnO_2/Sn Mott-Schottky heterojunction was modeled with 4 atomic layers of 4 × 4 Sn (1 1 2) and one atomic layer of 3 × 2 SnO_2(1 1 0). The sampling was employed for the Brillouin zone with 3 × 3 × 1 Monkhorst–Pack[16] meshes in all calculations. The self-consistent field (SCF) tolerance, the maximum displacement and the energy cut-off were set to "fine" with high accuracy of 1 × 10^{-6} eV and 400 eV. For each reaction step, the convergence criterion for optimizations was met and the largest remaining force on each atom was less than < 0.02 eV/Å.

Reaction mechanisms for the generation of formic acid (step 1) [17,18] and CO (step2) [19,20]are depicted below,

$$CO_2(g) + e^- + H^+ + * \rightarrow HCOO^* \quad (1\text{-}1)$$

$$HCOO^* + e^- + H^+ \rightarrow HCOOH^* \quad (1\text{-}2)$$

$$HCOOH^* \rightarrow HCOOH\ (aq) + * \quad (1\text{-}3)$$

$$CO_2(g) + e^- + H^+ + * \rightarrow COOH^* \quad (2\text{-}1)$$

$$^*COOH + e\text{-} + H+ \rightarrow HCOOH^* \quad (2\text{-}2)$$

$$COOH^* + e^- + H^+ \rightarrow CO^* + H_2O \quad (2\text{-}2)$$

$$CO^* \rightarrow CO\ (g) + * \quad (2\text{-}3)$$

where * represents the surface adsorption site.

The binding energies of the adsorbates on the SnO_2(110) surface and SnO_2/Sn Mott-Schottky heterojunction were calculated by

$$\Delta E_{ads} = E_{ads+sur} - (E_{ads}+E_{sur})$$

where $E_{ads+sur}$ represents the total energy of the adsorbate interacting with the surface, E_{ads} is the energy of the adsorbate in the gas phase, and E_{sur} is the energy of the bare surface.

The Gibbs free energy of H* (ΔG_H) were calculated by

$$\Delta G_H = \Delta E_{H*} + \Delta E_{ZPE} - T\Delta S$$

$$\Delta E_{H*} = E_{sur+H*} - (E_{H*}+E_{sur})$$

whereE_{sur+H*} and E_{sur} denote the energy of substrates with an adsorbed H atom and the energy of bare substrates. The free energy of electrochemical reduction of H_2 was calculated based on a computational hydrogen electrode (CHE) model, E_{H*} denotes half of the energy of H_2 [21], ΔZPE is the variation in zero-point energies, ZPE of adsorbed species have been calculated from frequencies obtained within the harmonic oscillator approximation. Vibrational contributions to the entropy of adsorbed species can also be obtained using the calculated vibrational frequencies. And ΔS is the change in entropy before and after the reaction. T is temperature and equals to 298 K. Therefore, the free energy of the adsorbed state can be taken as $\Delta G_H = \Delta E_{H*}$+0.24 eV. [22]. The adsorption energetics of the most stable states of the adsorbate on the modeled catalysts are shown in Table S1.

3. Results and discussion

The SnO_2/CF was synthesized by a one-step hydrothermal process at 120 °C, as illustrated in Scheme 1 (experimental details in the Supporting Information). The crystalline structure of SnO_2/CF was then characterized by XRD measurements. Three intense diffraction peaks emerged at 2θ = 26.61°, 33.89° and 51.78° (Fig. S1a), which can be indexed to the (110), (101) and (211) lattice planes of SnO_2 (PDF#41–1445), respectively, indicating the successful formation of SnO_2. XPS measurements (Fig. S1b-c) show a doublet at 487.2 and 495.7 eV, that can be ascribed to the Sn $3d_{3/2}$ and Sn $3d_{5/2}$ electrons of Sn^{4+}, in good agreement with the formation of SnO_2 in the sample.[23,24] Figure S1c shows the XPS profile of O 1 *s*, which can be deconvoluted into two peaks at 531.2 and 532.7 eV, corresponding to Sn^{4+}-O, and adsorbed oxygen, respectively.[25] The specific surface area of SnO_2/CF was determined to be 118.14 $m^2\ g^{-1}$ by nitrogen adsorption–desorption isotherms (Figure S1d), indicating its large surface area.[25-29]

The morphology of SnO_2/CF was then examined by scanning electron microscopy (SEM) measurements. As shown in Fig. 1a-c, carbon fibers were coated with a number of SnO_2 nanoparticles of ca. 200 nm in diameter. The coating of SnO_2 on unifocal carbon fiber promotes the electronic conductivity of the cathode and thus favors the CO_2R. Further structural insights were obtained in high-resolution transmission electron microscopy (HRTEM) measurements (Fig. 1d-e), where the nanoparticles exhibited well-defined lattice fringes with an interplanar spacing of 3.35 Å, due to the SnO_2(110) planes. Indeed, in the selected area electron diffraction (SAED) measurements (Fig. 1f), the diffraction patterns of SnO_2(110), (101), (200), (211), and (301) planes can be clearly identified.

It has been reported that SnO_2 can be converted into metallic Sn during the cathodic CO_2R process, leading to active debates about the catalytic active component.[30,31] Thus, to examine the structural dynamics of SnO_2/CF, the composite was subject to CO_2R at –1 V for 1 h and then characterized by XRD and HRTEM measurements. From Figure S2a, one can see that the intensity of the SnO_2 diffraction peaks was dramatically reduced and only very weak peaks remain. Concurrently, sharp diffraction peaks emerged at 2θ = 30.64°, 32.02°, 44.90°, consistent with the Sn (200), (101), (211) planes, respectively, indicating the reduction of SnO_2 to metallic Sn. This was also corroborated by results from TEM measurements (Fig. 1g-h), where lattice fringes of both SnO_2 (with an interplanar distance of 3.35 Å from SnO_2(110)) and Sn (with an interplanar distance of 2.92 Å from Sn (200)) can be observed, suggesting partial conversion of SnO_2 to Sn. Indeed in SAED measurements, the patterns of both SnO_2 and Sn can be readily identified (Fig. 1i).

The detailed transformation dynamics of SnO_2 to Sn during CO_2R at varied potentials were further examined by in situ Raman spectroscopy measurements. [5,32,33] From Fig. 2, the pristine SnO_2 can be seen to exhibit three vibrational bands at 113, 211 and 632 cm^{-1}, which are attributed to the B_{1g}, B_{2g} and A_{1g} modes of Sn-O, respectively.[34,35] At the applied potential of –0.2 and –0.4 V in CO_2-saturated electrolyte for CO_2R (Fig. 2a-b), these Raman peaks typical of SnO_2 remained well-resolved, with no obvious intensity attenuation at increasing reaction time. When the applied potential was further increased to –0.6 and –0.8 V, the B_{1g} and B_{2g} bands at 113 and 211 cm^{-1} disappeared after 30 min and the A_{1g} band started to attenuate (Fig. 2c-d). However, as shown in Fig. 2e, the A_{1g}, B_{1g} and B_{2g} Raman peaks all diminished markedly after CO_2R at a more negative potential of –1.0 V for 10 min and disappeared completely after 20 min, indicating that most of the SnO_2 had been converted to Sn. The evolution dynamics of SnO_2 at –1.0 V are further evidenced in Raman spectra acquired at a 1 min interval. From Fig. 2f, it can be observed that the A_{1g} Raman peak of SnO_2 became weakened but remained visible after CO_2R for 19 min, and then vanished into the baseline at prolonged reaction time.

The results from the in-situ Raman examination indicates the SnO_2 completely vanished after electrolysis of CO_2R, which contradicts with the results from XRD and TEM measurements (Fig. 1 and S2). This might be accounted for by that bulk SnO_2 might be partially converted into metallic Sn during CO_2R process, and only a very thin top layer of SnO_2 at the nanometer scale remains after

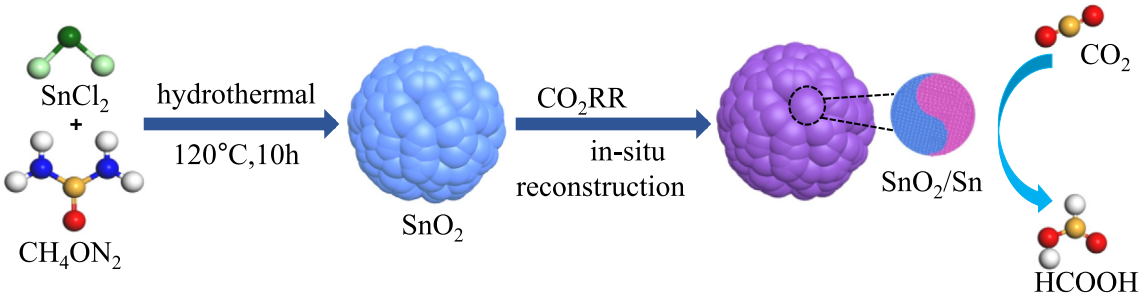

Scheme 1. Schematic illustration of the synthesis of SnO_2 nanoparticles on carbon cloth.

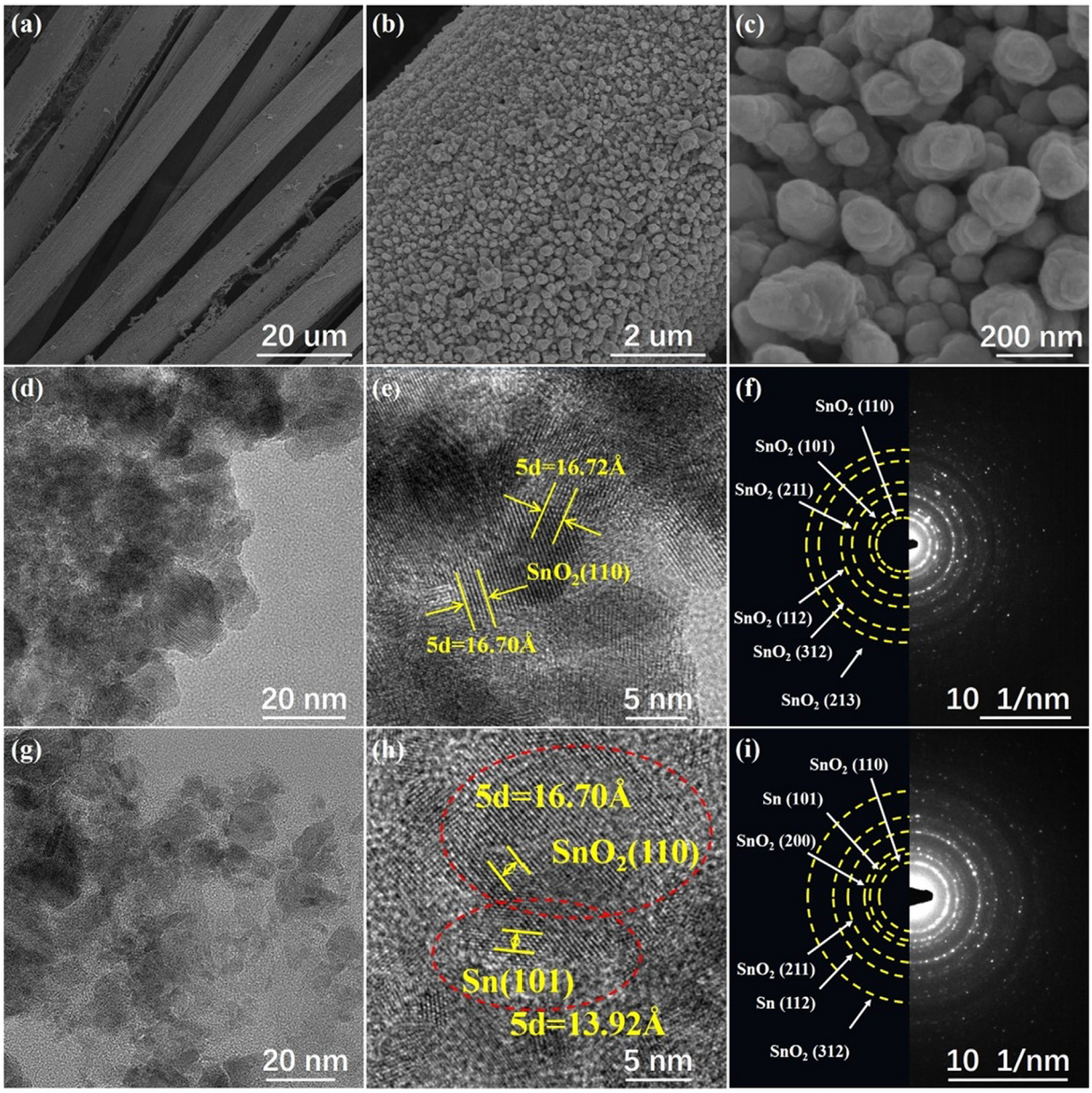

Fig. 1. (a-c) SEM images, (d,e) TEM images and (f) SAED patterns of as-prepared SnO_2/CF. (g,h) TEM images and (i) SAED patterns of spent SnO_2/CF for 1 h for CO_2R at –1 V.

CO_2R for 1 h, which cannot be well detected by Raman spectroscopy without surface-enhancing. However, HRTEM can well resolve the minimum amount of SnO_2 residue while and XRD can detect the presence of SnO_2 in bulk state. Thus, it is concluded that the in-situ formed SnO_2/Sn heterostructures were formed. These are likely the intrinsic active component for CO_2R at high reduction potentials. This hypothesis was supported by results from XPS measurements of the spent SnO_2/CF samples after CO_2R at –1.0 V for 1 h. As shown in Fig. S2b, the top surface of the spent SnO_2/CF is mainly composed of SnO_2, with a small fraction of Sn. At 10 nm below the surface by ion sputtering (Fig. S2c), the metallic Sn signal was enhanced whereas that of SnO_2 diminished concurrently. When the peeling depth reached 20 nm (Fig. S2d), only metallic Sn was observed, and no SnO_2 could be resolved. These suggest that SnO_2/Sn heterostructures were indeed in situ formed during CO_2R (Fig. S3), in good agreement with results from TEM and SAED measurements (Fig. 1g-i).

The electrocatalytic performance of SnO_2/CF towards CO_2R was first studied in an H-type electrochemical cell in a CO_2-saturated 0.5 M $KHCO_3$ solution by linear sweep voltammetry (LSV). As a control experiment, Sn/CF was also prepared by thermal reduction of SnO_2/CF (Fig. S3a) and the catalytic activity towards CO_2R was evaluated and compared (Fig. S4). From Fig. S4, SnO_2/CF can be seen to show a much higher current density in CO_2-saturated $KHCO_3$ solution than that in N_2-saturated electrolyte, indicating that SnO_2/CF is active towards CO_2R. The cathodic peak at –0.3 V vs RHE is likely due to the reduction of SnO_2 to metallic Sn. The FE of the products at each potential are shown in Fig. 3a. SnO_2/CF exhibits an FE of 44.45% for formate at low potentials and a maximum FE of 93.7% at –1.0 V. By contrast, Sn/CF exhibits a maximum FE of 57.87% for formate at –0.9 V. The partial current densities of the products by step electrolysis at each potential are shown in Fig. 3b and S5. Obviously, with the increase of the applied potential, the partial current density of formate increases sharply on SnO_2/CF, reaching a maximum of 40.8 mA cm^{-2}, about 3.2 times

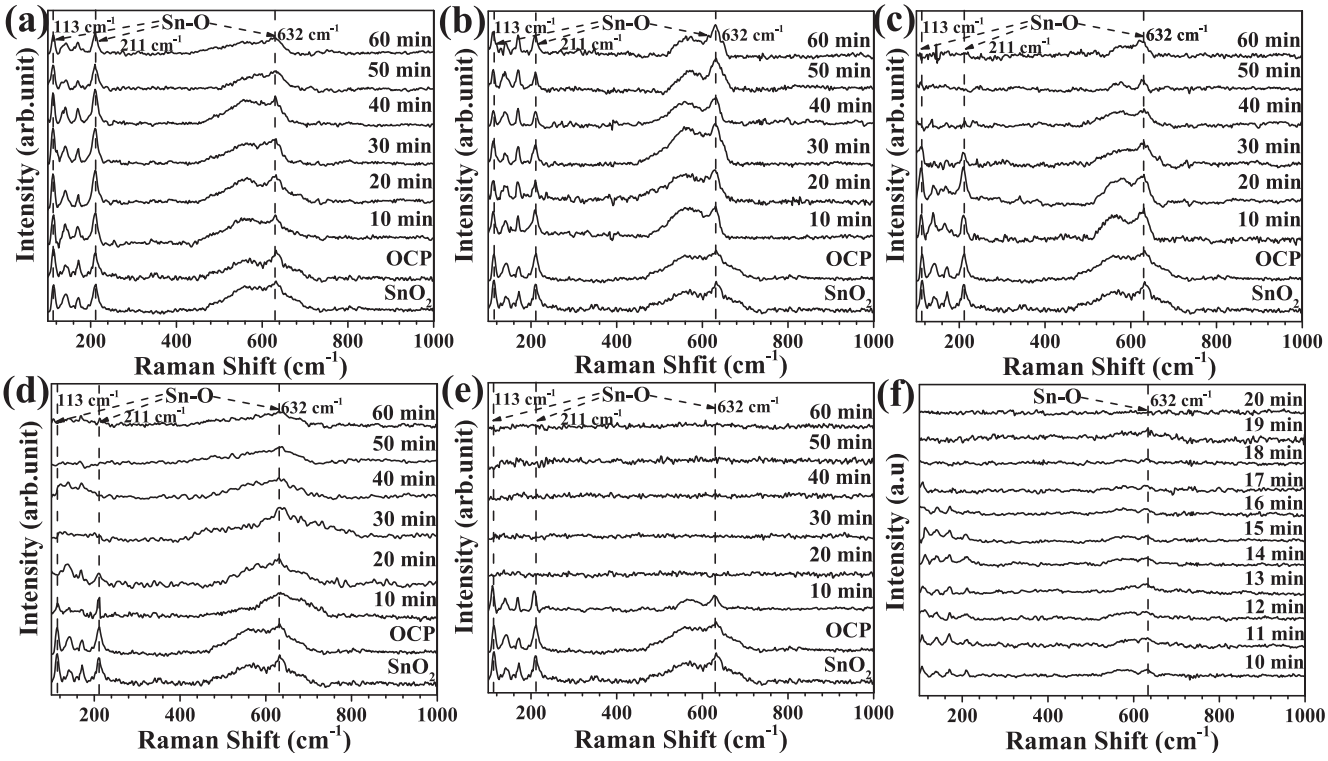

Fig. 2. In situ Raman spectra of SnO_2 at varied applied potentials (vs RHE): (a) –0.2 V, (b) –0.4 V, (c) –0.6 V, (d) –0.8 V, (e) –1.0 V, and (f) –1.0 V in 10 to 20 min for 1 h for CO_2R.

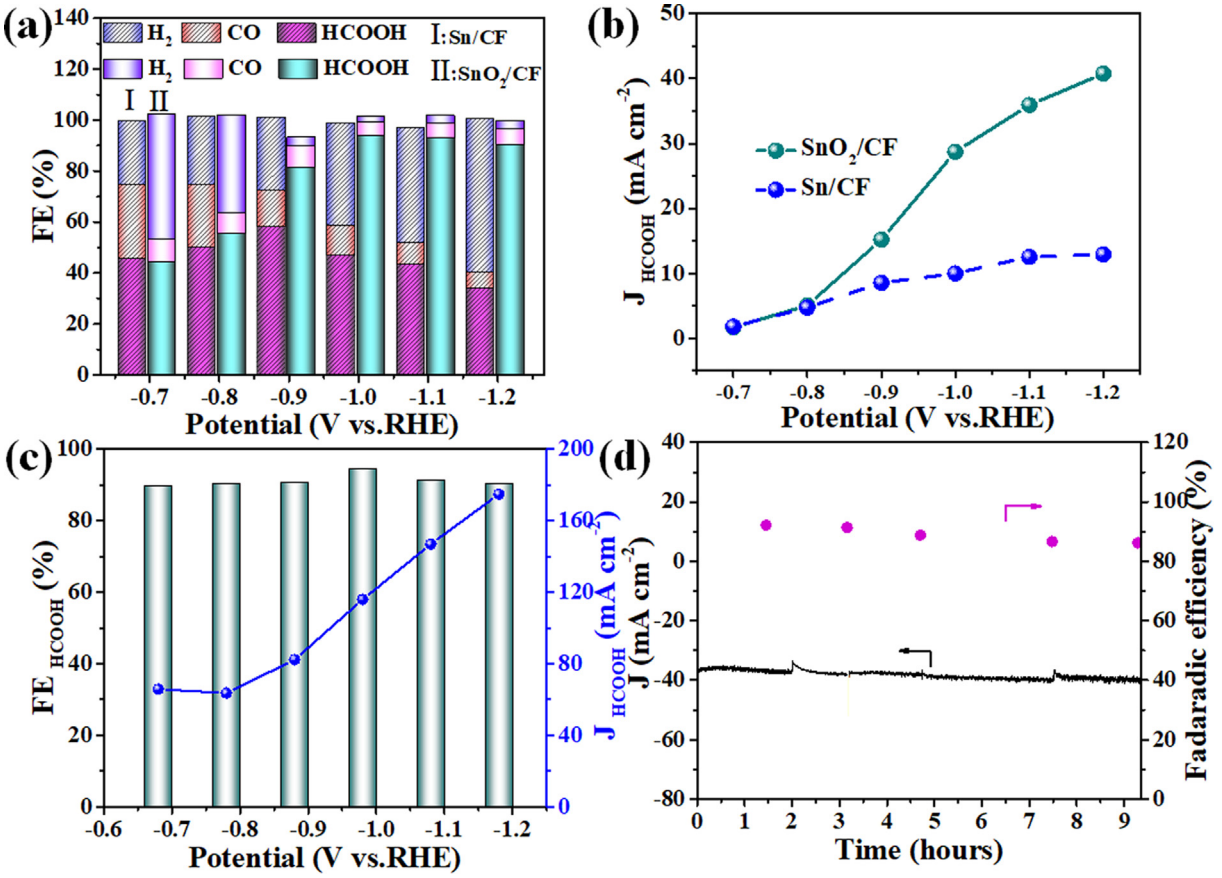

Fig. 3. (a) The FE of all products and (b) partial current density of formate on SnO_2/CF and Sn/CF at applied potentials from –0.7 to –1.2 V; (c) FE and partial current density of formate for CO_2R on SnO_2/CF in on a GDE in flow cell with 1 M KOH. (d) Stability test of SnO_2/CF at –1.1 V vs. RHE in 9 h.

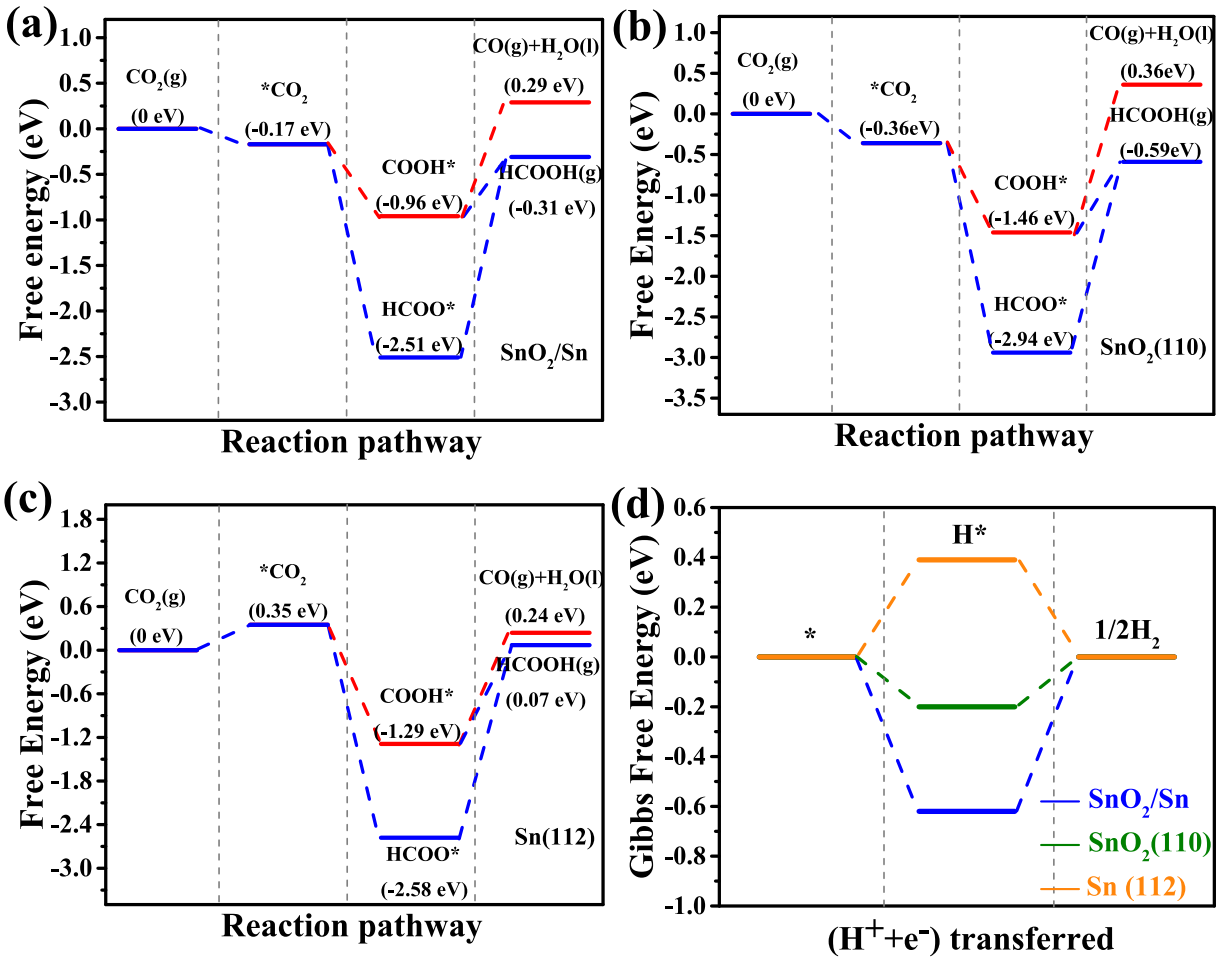

Fig. 4. Calculated free energy diagrams for the formation of formate and CO from CO_2R on (a) heterostructured SnO_2/Sn, (b) SnO_2 and (c)Sn, and (d) HER on Sn (1 1 2), SnO_2 (1 1 0) and SnO_2/Sn.

that of Sn/CF at −1.2 V, indicating the pure phase of Sn is less active than the heterostructured sample. The catalytic activity and selectivity of SnO_2/CF outperforms most of the reported Sn-based catalysts (Fig. S6 and Table S2).

The intrinsic activity of SnO_2/CF was evaluated by normalizing the partial current density of the products to the electrochemical surface area (ECSA), which was determined by the double layer capacitance (Fig. S7a-c). From Fig. S7d-e, one can see that SnO_2/CF exhibits only a low partial current density for H_2 and CO, indicating that the hydrogen evolution and CO production were effectively suppressed. The partial current density for formate reaches 188.6 μA cm^{-2}, about 3.7 times that of Sn/CF at −1.2 V, and is comparable to leading catalysts reported in the literature.[26,36] The kinetics of CO_2R on SnO_2/CF catalysts were then evaluated by Tafel analysis. As demonstrated in Fig. S7f, SnO_2/CF and Sn/CF catalysts exhibit a Tafel slop of 206.6 mV•dec^{-1} and 250.0 mV•dec^{-1}, which indicates much faster reaction kinetics of CO_2R on the former catalyst than the latter.[37,38] SnO_2/CF also exhibited excellent stability (Fig. 3d), with only a negligible current decay and a steady FE over 85% in the continuous electrolysis for 9 h.

Due to the limited solubility of CO_2 in aqueous solutions, it is difficult to achieve high current density for CO_2R and only neutral electrolyte can be used in an H-type cell. However, it has been reported that hydrogen evolution reaction, the competing reaction to CO_2R, can be suppressed and the activation energy battier for CO_2R can be reduced in alkaline electrolyte. Thus, the catalytic activity of SnO_2/CF catalyst was also examined on a gas diffusion electrode (GED) in a flow cell, with 1 M KOH electrolyte. Fig. 3c displays the partial current densities and FEs of formate at various cathodic potentials, which can reach 174.86 mA cm^{-2} at − 1.18 V, 4 times that in an H-type cell (40.76 mA cm^{-2}). Meanwhile, a high FE of more than 93% was obtained for formate at the current density of 118 mA cm^{-2} at − 0.98 V. Again, the remarkable CO_2R activity of SnO_2/CF might be ascribed to the in-situ formation of SnO_2/Sn heterostructures. To demonstrate this point, the catalytic performance of SnO_2/CF was also examined by applying potential pulses, where relatively low partial current density for formate was observed (Fig. S9), as the oxide state of SnO_2 was retained during CO_2R.

To further understand the superior performance and unraveling the reaction mechanism of CO_2R on SnO_2/CF, density functional theory (DFT) calculations were carried out. Note that SnO_2 was partially reduced to Sn and exhibits a SnO_2/Sn heterostructure under the CO_2R conditions, as manifested in XPS, in situ Raman and HRTEM measurements.[39] The Mott-Schottky heterostructure of SnO_2/Sn was modeled by using a Sn substrate with a SnO_2 layer and the adsorption energetics of the CO_2R intermediates were evaluated and compared with that on pure Sn and SnO_2 (Fig. S10). Note that both HCOO* and COOH* are key intermediate for formate, respectively.[17,33,40] The Gibbs free energy of CO_2R intermediates to CO and formate on the three models are shown in Fig. 4a–c and S11-13. The free energy barrier (ΔG) of COOH* to HCOOH is observed on SnO_2/Sn (0.65 eV), SnO_2(0.87 eV) and Sn (1.22 eV), respectively, indicating that the path for formate produc-

tion is favored energetically on heterostructured SnO_2/Sn than on pure SnO_2 and Sn. As hydrogen evolution reaction is competitive to CO_2R and protons for formate formation comes from water dissociation,[41,42] the adsorption energy of protons also plays a critical role in the dynamics of CO_2R to formate. As shown in Fig. 4d, the Gibbs free energy of hydrogen (ΔG_H) on SnO_2, Sn and SnO_2/Sn were calculated to be –0.20, 0.39 and –0.62 eV, respectively. The Gibbs free energy of H on Sn is positive, indicating that H adsorption is not favored and both HER and formate production are relatively not favored, since CO_2R to formate need adsorbed H too. While the Gibbs free energy of H on SnO_2 and SnO_2/Sn are both negative and the it is more positive on SnO_2 than SnO_2/Sn heterostructure, it suggests that HER process is more prominent on Sn than SnO_2/Sn structure and the formate production is more favored on SnO_2/Sn structure than Sn. Experimentally, it observed that formate production is more active on SnO_2/Sn than SnO_2, thus, indicating that the enhanced adsorption of H on SnO_2/Sn is not strong enough to compete with CO_2 adsorption and reduction.[36,43-45] DFT calculation also indicated that SnO_2 in SnO_2/Sn heterostructure than is apparently strained as compared to the pure SnO_2, which might be responsible for the favored energetics of formate production of the heterostructure.

4. Conclusion

In summary, tin oxide nanoparticles were grown onto carbon cloth by a facile hydrothermal method. During the CO_2R electrocatalysis in $KHCO_3$, SnO_2/Sn Mott–Schottky heterojunctions were formed, as evidenced in HRTEM, XPS and in situ Raman spectroscopy measurements, leading to a high Faraday efficiency of 93.6% at –1.0 V, along with a partial current density of 28.7 mA cm^{-2} that maintained good stability for 9 h at –1.1 V in an H-type cell and 118 mA cm^{-2} in 1 M KOH electrolyte in a flow cell. DFT calculations indicate that the formate production is more energetically favored on SnO_2/Sn heterostructures and hydrogen evolution was suppressed, possible due to the strain on SnO_2 oxide induced by the heterostructure. Results from this work highlight the dynamic nature of SnO_2 catalysts during CO_2R and shed light on the mechanistic origin of the enhanced electrocatalytic performance. Such fundamental insights may be exploited for the design and engineering of high-performance CO_2RR catalysts.

Notes

The authors declare no competing financial interest.

Declaration of Competing Interest

The authors declare that they have no known competing financial interests or personal relationships that could have appeared to influence the work reported in this paper.

Acknowledgements

This work was supported by the National Natural Science Foundation of China (No. U2032151 and 21773224), National Key R&D Program of China (No. 2018YFB1502600) and the Fundamental Research Funds for Central Universities (SCUT Grant No. 2019ZD22) and Development Program of Guangdong Province (No.2019B110209002).

Appendix A. Supplementary material

Supplementary data to this article can be found online at https://doi.org/10.1016/j.jcat.2021.04.028.

References

[1] Y.-X. Duan, F.-L. Meng, K.-H. Liu, S.-S. Yi, S.-J. Li, J.-M. Yan, Q. Jiang, Amorphizing of Cu Nanoparticles toward Highly Efficient and Robust Electrocatalyst for CO_2 Reduction to Liquid Fuels with High Faradaic Efficiencies, Adv. Mater. 30 (2018) 1706194.
[2] B. Jiang, X.-G. Zhang, K. Jiang, D.-Y. Wu, W.-B. Cai, Boosting Formate Production in Electrocatalytic CO_2 Reduction over Wide Potential Window on Pd Surfaces, J. Am. Chem. Soc. 140 (2018) 2880–2889.
[3] L. Dai, Q. Qin, P. Wang, X. Zhao, C. Hu, P. Liu, R. Qin, M. Chen, D. Ou, C. Xu, S. Mo, B. Wu, G. Fu, P. Zhang, N. Zheng, Ultrastable atomic copper nanosheets for selective electrochemical reduction of carbon dioxide, Sci. Adv. 3 (2017) e1701069.
[4] G.A. El-Nagar, K.M. Dawood, M.S. El-Deab, B.E. Al-Andouli, Efficient direct formic acid fuel cell (DFAFC) anode of nano-sized palladium complex: High durability and activity origin, Appl. Catal. B. 213 (2017) 118–126.
[5] W. Luc, C. Collins, S. Wang, H. Xin, K. He, Y. Kang, F. Jiao, Ag–Sn Bimetallic Catalyst with a Core-Shell Structure for CO_2 Reduction, J. Am. Chem. Soc. 139 (2017) 1885–1893.
[6] Q. Gong, P. Ding, M. Xu, X. Zhu, M. Wang, J. Deng, Q. Ma, N. Han, Y. Zhu, J. Lu, Z. Feng, Y. Li, W. Zhou, Y. Li, Structural defects on converted bismuth oxide nanotubes enable highly active electrocatalysis of carbon dioxide reduction, Nat. Commun. 10 (2019) 2807.
[7] L. Xu, W. Zeng, Y. Li, Synthesis of morphology and size-controllable SnO_2 hierarchical structures and their gas-sensing performance, Appl. Surf. Sci. 457 (2018) 1064–1071.
[8] Z. Yiliguma, C. Wang, A. Yang, L. Guan, A.M. Shang, L. Al-Enizi, G. Zhang, Zheng, Sub-5 nm SnO_2 chemically coupled hollow carbon spheres for efficient electrocatalytic CO_2 reduction, J. Mater. Chem. A. 6 (2018) 20121–20127.
[9] N. Han, Y. Wang, J. Deng, J. Zhou, Y. Wu, H. Yang, P. Ding, Y. Li, Self-templated synthesis of hierarchical mesoporous SnO_2 nanosheets for selective CO_2 reduction, J. Mater. Chem. A. 7 (2019) 1267–1272.
[10] B. Kumar, V. Atla, J.P. Brian, S. Kumari, T.Q. Nguyen, M. Sunkara, J.M. Spurgeon, Reduced SnO_2 Porous Nanowires with a High Density of Grain Boundaries as Catalysts for Efficient Electrochemical CO_2-into-HCOOH Conversion, Angew. Chem., Int. Ed. 56 (2017) 3645–3649.
[11] Y. Chen, M.W. Kanan, Tin Oxide Dependence of the CO_2 Reduction Efficiency on Tin Electrodes and Enhanced Activity for Tin/Tin Oxide Thin-Film Catalysts, J. Am. Chem. Soc. 134 (2012) 1986–1989.
[12] H. Liu, X. Liu, W. Yang, M. Shen, S. Geng, C. Yu, B. Shen, Y. Yu, Photocatalytic dehydrogenation of formic acid promoted by a superior PdAg@g-C_3N_4 Mott-Schottky heterojunction, J. Mater. Chem. A 7 (2019) 2022–2026.
[13] S.J. Clark, M.D. Segall, C.J. Pickard, P.J. Hasnip, M.I.J. Probert, K. Refson, M.C. Payne, First principles methods using CASTEP, Zeitschrift für Kristallographie - Crystalline Materials 220 (2005) 567–570.
[14] S. Grimme, J. Antony, S. Ehrlich, H. Krieg, A consistent and accurate ab initio parametrization of density functional dispersion correction (DFT-D) for the 94 elements H-Pu, J. Chem. Phys. 132 (2010) 154104.
[15] J.P. Perdew, K. Burke, M. Ernzerhof, Generalized Gradient Approximation Made Simple, Phys. Rev. Lett. 77 (1996) 3865–3868.
[16] M. Methfessel, A.T. Paxton, High-precision sampling for Brillouin-zone integration in metals, Phys. Rev. B. 40 (1989) 3616–3621.
[17] J.S. Yoo, R. Christensen, T. Vegge, J.K. Nørskov, F. Studt, Theoretical Insight into the Trends that Guide the Electrochemical Reduction of Carbon Dioxide to Formic Acid, ChemSusChem 9 (2016) 358–363.
[18] H. Huang, H. Jia, Z. Liu, P. Gao, J. Zhao, Z. Luo, J. Yang, J. Zeng, Understanding of Strain Effects in the Electrochemical Reduction of CO_2: Using Pd Nanostructures as an Ideal Platform, Angew. Chem., Int. Ed. 56 (2017) 3594–3598.
[19] S. Sarfraz, A.T. Garcia-Esparza, A. Jedidi, L. Cavallo, K. Takanabe, Cu–Sn Bimetallic Catalyst for Selective Aqueous Electroreduction of CO_2 to CO, ACS Catal. 6 (2016) 2842–2851.
[20] S. Zhu, B. Jiang, W.-B. Cai, M. Shao, Direct Observation on Reaction Intermediates and the Role of Bicarbonate Anions in CO_2 Electrochemical Reduction Reaction on Cu Surfaces, J. Am. Chem. Soc. 139 (2017) 15664–15667.
[21] A.A. Peterson, F. Abild-Pedersen, F. Studt, J. Rossmeisl, J.K. Nørskov, How copper catalyzes the electroreduction of carbon dioxide into hydrocarbon fuels, Energy Environ. Sci. 3 (2010) 1311–1315.
[22] C. Ling, X. Niu, Q. Li, A. Du, J. Wang, Metal-Free Single Atom Catalyst for N_2 Fixation Driven by Visible Light, J. Am. Chem. Soc. 140 (2018) 14161–14168.
[23] S. Liu, J. Xiao, X.F. Lu, J. Wang, X. Wang, X.W. Lou, Efficient Electrochemical Reduction of CO_2 to HCOOH over Sub-2 nm SnO_2 Quantum Wires with Exposed Grain Boundaries, Angew. Chem., Int. Ed. 58 (2019) 8499–8503.
[24] C. Hu, L. Li, W. Deng, G. Zhang, W. Zhu, X. Yuan, L. Zhang, Z.-J. Zhao, J. Gong, Selective Electroreduction of Carbon Dioxide over SnO_2-Nanodot Catalysts, ChemSusChem 13 (2020) 6353–6359.
[25] H. Li, N. Xiao, Y. Wang, C. Liu, S. Zhang, H. Zhang, J. Bai, J. Xiao, C. Li, Z. Guo, S. Zhao, J. Qiu, Promoting the electroreduction of CO_2 with oxygen vacancies on a plasma-activated SnO_x/carbon foam monolithic electrode, J. Mater. Chem. A. 8 (2020) 1779–1786.
[26] G. Liu, Z. Li, J. Shi, K. Sun, Y. Ji, Z. Wang, Y. Qiu, Y. Liu, Z. Wang, P. Hu, Black reduced porous SnO_2 nanosheets for CO_2 electroreduction with high formate selectivity and low overpotential, Appl. Catal. B. 260 (2020) 118134.

[27] F. Li, L. Chen, G.P. Knowles, D.R. MacFarlane, J. Zhang, Hierarchical Mesoporous SnO_2 Nanosheets on Carbon Cloth: A Robust and Flexible Electrocatalyst for CO_2 Reduction with High Efficiency and Selectivity, Angew. Chem., Int. Ed. 56 (2017) 505–509.
[28] L. Fan, Z. Xia, M. Xu, Y. Lu, Z. Li, 1D SnO_2 with Wire-in-Tube Architectures for Highly Selective Electrochemical Reduction of CO2 to C1 Products, Adv. Funct. Mater. 28 (2018) 1706289.
[29] H. Ge, Z. Gu, P. Han, H. Shen, A.M. Al-Enizi, L. Zhang, G. Zheng, Mesoporous tin oxide for electrocatalytic CO_2 reduction, J. Colloid Sci. 531 (2018) 564–569.
[30] J.E. Pander, M.F. Baruch, A.B. Bocarsly, Probing the Mechanism of Aqueous CO_2 Reduction on Post-Transition-Metal Electrodes using ATR-IR Spectroelectrochemistry, ACS Catal. 6 (2016) 7824–7833.
[31] M. Batzill, K. Katsiev, U. Diebold, Surface morphologies of SnO2(110), Surf. Sci. 529 (2003) 295–311.
[32] K. Ye, Z. Zhou, J. Shao, L. Lin, D. Gao, N. Ta, R. Si, G. Wang, X. Bao, In Situ Reconstruction of a Hierarchical Sn-Cu/SnOx Core/Shell Catalyst for High-Performance CO_2 Electroreduction, Angew. Chem., Int. Ed. 59 (2020) 4814–4821.
[33] J.T. Feaster, C. Shi, E.R. Cave, T. Hatsukade, D.N. Abram, K.P. Kuhl, C. Hahn, J.K. Nørskov, T.F. Jaramillo, Understanding Selectivity for the Electrochemical Reduction of Carbon Dioxide to Formic Acid and Carbon Monoxide on Metal Electrodes, ACS Catal. 7 (2017) 4822–4827.
[34] A. Dutta, A. Kuzume, M. Rahaman, S. Vesztergom, P. Broekmann, Monitoring the Chemical State of Catalysts for CO_2 Electroreduction: An In Operando Study, ACS Catal. 5 (2015) 7498–7502.
[35] C. Li, M. Zheng, X. Wang, L. Yao, L. Ma, W. Shen, Fabrication and ultraviolet photoresponse characteristics of ordered SnO_x($x \approx 0.87, 1.45, 2$) nanopore films, Nanoscale Res. Lett. 6 (2011) 615.
[36] J. Wang, J. Zou, X. Hu, S. Ning, X. Wang, X. Kang, S. Chen, Heterostructured intermetallic CuSn catalysts: high performance towards the electrochemical reduction of CO_2 to formate, J. Mater. Chem. A. 7 (2019) 27514–27521.
[37] M. Dunwell, W. Luc, Y. Yan, F. Jiao, B. Xu, Understanding Surface-Mediated Electrochemical Reactions: CO_2 Reduction and Beyond, ACS Catal. 8 (2018) 8121–8129.
[38] J. Rosen, G.S. Hutchings, Q. Lu, S. Rivera, Y. Zhou, D.G. Vlachos, F. Jiao, Mechanistic Insights into the Electrochemical Reduction of CO_2 to CO on Nanostructured Ag Surfaces, ACS Catal. 5 (2015) 4293–4299.
[39] Y. Deng, B.S. Yeo, Characterization of Electrocatalytic Water Splitting and CO_2 Reduction Reactions Using In Situ/Operando Raman Spectroscopy, ACS Catal. 7 (2017) 7873–7889.
[40] R. Kortlever, J. Shen, K.J.P. Schouten, F. Calle-Vallejo, M.T.M. Koper, Catalysts and Reaction Pathways for the Electrochemical Reduction of Carbon Dioxide, J. Phys. Chem. Lett. 6 (2015) 4073–4082.
[41] W. Ma, S. Xie, X.-G. Zhang, F. Sun, J. Kang, Z. Jiang, Q. Zhang, D.-Y. Wu, Y. Wang, Promoting electrocatalytic CO_2 reduction to formate via sulfur-boosting water activation on indium surfaces, Nat. Commun. 10 (2019) 892.
[42] D. Strmcnik, P.P. Lopes, B. Genorio, V.R. Stamenkovic, N.M. Markovic, Design principles for hydrogen evolution reaction catalyst materials, Nano Energy 29 (2016) 29–36.
[43] N. Han, Y. Wang, H. Yang, J. Deng, J. Wu, Y. Li, Y. Li, Ultrathin bismuth nanosheets from in situ topotactic transformation for selective electrocatalytic CO_2 reduction to formate, Nat. Commun. 9 (2018) 1320.
[44] L.-F. Shen, B.-A. Lu, Y.-Y. Li, J. Liu, Z.-C. Huang-fu, H. Peng, J.-Y. Ye, X.-M. Qu, J.-M. Zhang, G. Li, W.-B. Cai, Y.-X. Jiang, S.-G. Sun, Interfacial Structure of Water as a New Descriptor of the Hydrogen Evolution Reaction, Angew. Chem., Int. Ed. 59 (2020) 22397–22402.
[45] P. An, L. Wei, H. Li, B. Yang, K. Liu, J. Fu, H. Li, H. Liu, J. Hu, Y.-R. Lu, H. Pan, T.-S. Chan, N. Zhang, M. Liu, Enhancing CO_2 reduction by suppressing hydrogen evolution with polytetrafluoroethylene protected copper nanoneedles, J. Mater. Chem. A 8 (2020) 15936–15941.